Scalable synthesis of Cu-cluster catalysts via spark ablation for the electrochemical conversion of CO_2 to acetaldehyde

Koolen, Cedric David; Pedersen, Jack Kirk; Zijlstra, Bernardus; Winzely, Maximilian; Vrijburg, Wilbert; Kuddusi, Yasemen; Herranz, Juan; Schmidt-Ott, Andreas; Luo, Wen; Zuettel, Andreas

DOI
10.1038/s44160-024-00705-3

Publication date
2025

Document Version
Final published version

Published in
Nature Synthesis

nature synthesis

Article

https://doi.org/10.1038/s44160-024-00705-3

Scalable synthesis of Cu-cluster catalysts via spark ablation for the electrochemical conversion of CO_2 to acetaldehyde

Received: 17 July 2024

Accepted: 19 November 2024

Published online: 03 January 2025

Check for updates

Cedric David Koolen[1,2] ✉, Jack Kirk Pedersen[3] ✉, Bernardus Zijlstra[4], Maximilian Winzely[5], Jie Zhang[1], Tobias V. Pfeiffer[4], Wilbert Vrijburg[4], Mo Li[1], Ayush Agarwal[5,6], Zohreh Akbari[1,2], Yasemen Kuddusi[1,2], Juan Herranz[5], Olga V. Safonova[5], Andreas Schmidt-Ott[4,7], Wen Luo[8] ✉ & Andreas Zuettel[1,2]

The electrochemical conversion of CO_2 into acetaldehyde offers a sustainable and green alternative to the Wacker process. However, current electrocatalysts cannot effectively compete with heterogeneous processes owing to their limited selectivity towards acetaldehyde, resulting in low energy efficiencies. Here we report a theory-guided synthesis of a series of Cu-cluster catalysts (~1.6 nm) immobilized on various heteroatom-doped carbonaceous supports, produced via spark ablation of Cu electrodes (2.6 μg h^{-1} production rate, 6 Wh energy consumption). These catalysts achieve acetaldehyde selectivity of up to 92% at only 600 mV from the equilibrium potential. In addition, the catalysts exhibit exceptional catalytic stability during a rigorous 30 h stress test involving three repeated start–stop cycles. In situ X-ray absorption spectroscopy reveals that the initial oxide clusters were completely reduced under cathodic potential and maintained their metallic nature even after exposure to air, explaining the stable performance of the catalyst. First-principles simulations further elucidate a possible mechanism of CO_2 conversion to acetaldehyde.

The electrification of the chemical industry is needed for a complete and unambiguous energy transition[1]. Many processes depend heavily on the petrochemical industry, which are neither green nor energy efficient. One notable example of such processes is the well-known homogeneously catalysed production of acetaldehyde, a base chemical used in the production of drugs, dyes and fragrances[2]. Commercialized as the Wacker process, the Pd(II)-catalysed oxidation of ethylene to acetaldehyde dominates the global acetaldehyde market, which is valued at over 1.2 billion USD[3–5]. This process not only uses a feedstock from oil cracking (that is, ethylene) but also requires large amounts of hydrochloric acid to achieve the required conversions[4,5]. Although reliable, overcoming the limitations of this resource-intensive process is needed for a sustainable supply of acetaldehyde in the long term. Attempts have been made to heterogeneously convert ethylene to acetaldehyde using Pd–Cu zeolite catalysts with fixed acid sites on the support, which notably reduced the environmental toll of the process[6].

[1]Laboratory of Materials for Renewable Energy, Institute of Chemical Sciences and Engineering, Basic Science Faculty, École polytechnique fédérale de Lausanne Valais/Wallis, Energypolis, Sion, Switzerland. [2]Empa Materials Science and Technology, Dübendorf, Switzerland. [3]Center for High Entropy Alloy Catalysis, Department of Chemistry, University of Copenhagen, Copenhagen, Denmark. [4]VSPARTICLE B.V., Delft, the Netherlands. [5]Paul Scherrer Institute, PSI Center for Energy and Environmental Sciences, Villigen PSI, Villigen, Switzerland. [6]Environmental Engineering Institute, School of Architecture, Civil and Environmental Engineering, École Polytechnique Fédérale de Lausanne, Lausanne, Switzerland. [7]Faculty of Applied Sciences, Technical University of Delft, Delft, the Netherlands. [8]School of Environmental and Chemical Engineering, Shanghai University, Shanghai, China. ✉e-mail: cedric.koolen@epfl.ch; jack.k.pedersen@chem.ku.dk; wenluo@shu.edu.cn

https://doi.org/10.1038/s44160-024-00705-3

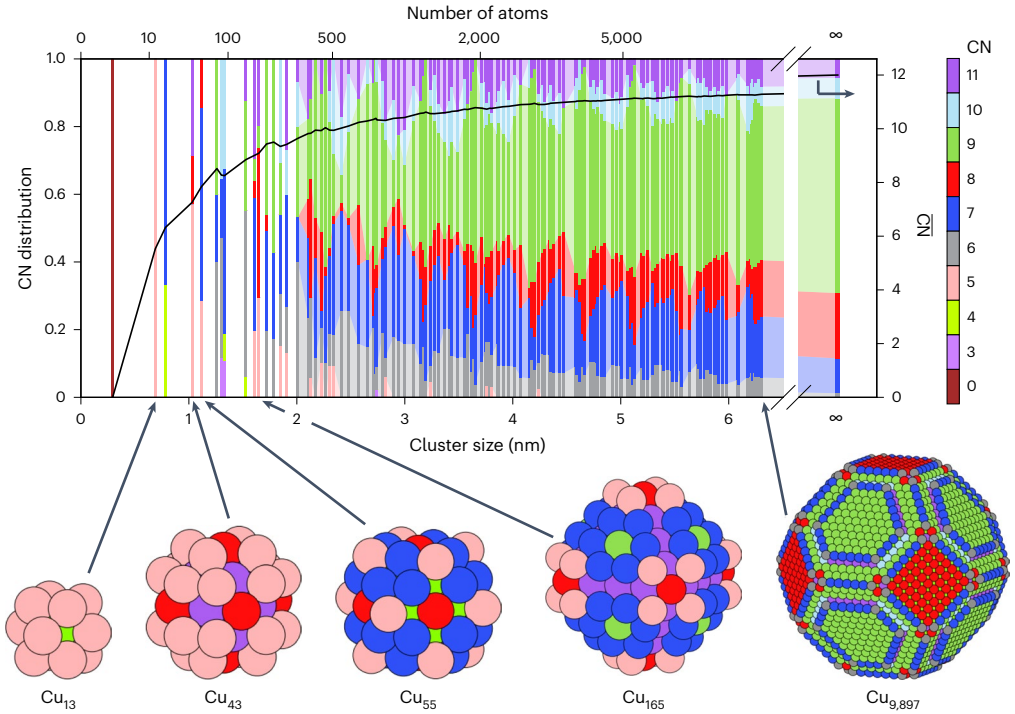

Fig. 1 | Computational catalyst screening. Wulf constructs of an infinitely large Cu crystal at equilibrium up to a single atom with the surface atom CN and overall average CN as a function of the cluster size. Only for particles <2 nm does discretization take place and particles with unique active sites and atomicity become apparent. The active site of CN 11 associated with Cu(110) and like surfaces is depicted in purple, showing the highest prevalence in Cu_{43} and Cu_{165}.

However, such methods still rely on petrochemically sourced ethylene and the acetaldehyde selectivity is not yet at par with the Wacker process. Here, we propose a fully green and carbon-neutral process instead to selectively produce acetaldehyde electrochemically using CO_2 as a resource.

The electrochemical CO_2 reduction reaction (CO_2RR) is a technology of industrial relevance that kills two birds with one stone: (1) it has the ability to substantially reduce our CO_2 footprint by fixating it in useful products, and (2) it tackles the intermittence problem associated with renewable energy by storing energy in chemical bonds[7]. However, CO_2RR faces important challenges[8]. Although high-value products, such as ethanol, ethylene and acetaldehyde, can be produced on Cu-based catalysts[9], polycrystalline Cu shows low selectivity for specific products and, thus, results in large energy losses[10]. Previous studies have shown that specific Cu surfaces have activities for certain products, that is, Cu(111) surfaces primarily produce CH_4, Cu(100) surfaces predominantly generate ethylene and Cu(110) surfaces mainly form oxygenates, such as ethanol[11–14]. Furthermore, defects, steps, kinks and edge sites have also shown preferentiality towards specific pathways[15–17]. Therefore, tremendous efforts have been devoted to engineer Cu electrodes to expose specific facets, defects and/or interfaces, to produce targeted products with unitary selectivity[18–22]. Also, attempts have been made to mix other elements with Cu to form bimetallic catalysts to tune the electronic nature and enhance the selectivity[23–27]. Unfortunately, achieving selectivity over 50% for oxygenates, in particular acetaldehyde, has proven to be challenging[20,26].

Recently, Cu clusters with particle sizes of less than 2 nm have emerged as an opportunity to refine the definition of the catalyst's active site by controlling the atomicity[28]. This has led to a successful enhancement of the CO_2RR selectivity towards ethanol to an industrial relevance (>90%)[29–31]. Inspired by these early successes, we have developed a theory-coupled-synthesis platform for the identification and synthesis of target Cu clusters with high selectivity for acetaldehyde, with the aim of exploring the potential of CO_2RR in replacing the commercial Wacker process.

Guided by theoretical simulations, we synthesized and evaluated the performance of a series of Cu(−Ag)cluster catalysts of <2 nm and achieved 92% selectivity for acetaldehyde at only 560 mV from the equilibrium potential (60 mV versus reversible hydrogen electrode (RHE)). Furthermore, by excluding the effect of support[29–31], and composition (pure Cu versus CuAg), we confirmed that cluster atomicity is the key factor in differentiating between CO_2RR pathways. We believe our platform offers a scalable and high-throughput catalyst design strategy to control cluster atomicity, composition and loading, which enables fast target identification and hit optimization for the selective electrosynthesis of base chemicals.

Results and discussion

Cluster selection

As the Cu(110) surface has been proven to be the most selective facet for acetaldehyde[13,14], we selected our target cluster on the basis of similarity to the infinite surface, that is, with the same proposed active site (coordination number (CN) of 11)[32]. We achieved this by a high-throughput method where we compared the CN of the target cluster (determined as a Wulf construct) with that of the infinite surface (Fig. 1)[33,34]. For clusters smaller than 2 nm, the distribution of surface CNs deviates notably from that of the bulk. Interestingly, over 30% of the surface atoms in the Cu_{43} and Cu_{165} clusters (with dimensions of approximately 1.0 nm and 1.6 nm, respectively) have a CN value of 11, similar to Cu(110). Therefore, we selected these clusters as our initial targets. Furthermore, as we have shown that adding Ag to Cu could enhance the selectivity of various shapes of Cu nanocrystals to oxygenates[27], we extended our target selection to include Cu-rich Cu–Ag clusters (with less than 20 at.% Ag).

Production of the Cu-cluster precatalysts

To avoid the influence of organic ligands and/or solvents on the physical and chemical properties of the clusters, we use spark ablation[35], a physical deposition method that is scalable, to synthesize our Cu(−Ag) clusters (Fig. 2). In brief, a power source is applied to two hollow metal electrodes (Cu and Cu, or Cu and Ag) separated by a gap through which

https://doi.org/10.1038/s44160-024-00705-3

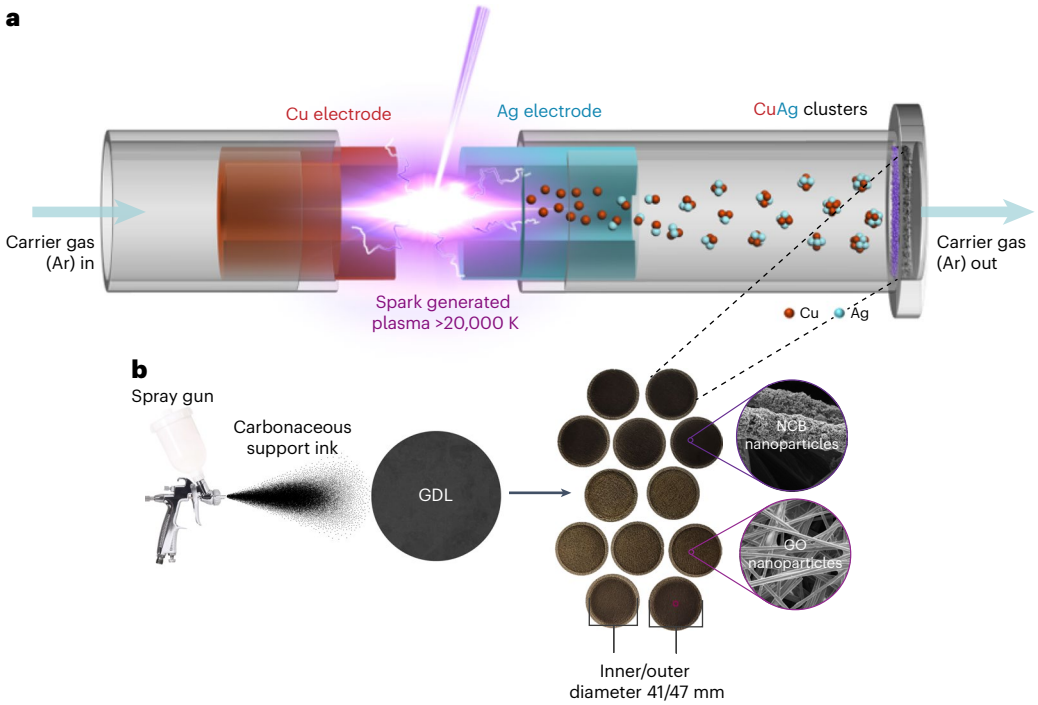

Fig. 2 | Scalable and atomically precise catalyst synthesis via spark ablation. a,**b**, Schematics of the spark ablation (**a**) and the immobilization (**b**) of Cu(−Ag) cluster precatalysts on heteroatom-doped carbonaceous supports (nanoparticles of NCB or GO) airbrushed on the gas difusion layer (GDL) substrates. Credit: spray gun and ink cloud, Adobe Inc.

a carrier gas (Ar) is flowed (Fig. 2a). Upon the breakdown of the potential, Ar is briefly ionized and becomes conductive, creating a plasma pulse with a temperature of more than 20,000 K and a pulse duration in the microsecond range[36]. By controlling the gas flow rate, repetition frequency and energy per spark, the electrode ablation rate can be controlled, producing an aerosol of clusters of well-defined size and composition[37,38]. However, the high degree of undercoordination of the produced cluster makes them extremely susceptible to agglomeration. Therefore, a selection of heteroatom-doped carbonaceous supports, that is, graphene oxide (GO) and N-doped carbon black (NCB) nanoparticles were synthesized and used to immobilize the clusters[39,40]. To this end, a commercial gas diffusion layer (GDL) was airbrushed with an optimized loading (high coverage without blocking the pores) of the carbonaceous support and used as a filter to collect the clusters from the aerosol stream (Fig. 2b). For information regarding the synthesis of the catalyst supports, see Supplementary Note 1 and Supplementary Fig. 1. For details on the cluster production, see Extended Data Fig. 1, Supplementary Note 2 and Supplementary Figs. 2 and 3. For details on the cluster immobilization, see Supplementary Notes 3–5 and Supplementary Figs. 5–11. For details on the cathode production process, see Supplementary Note 6 and Supplementary Figs. 12–16.

Four gas diffusion electrodes with ~0.1 wt.% metal loading (as based on the mass of airbrushed carbonaceous support, 0.4 $\mu g_{Cu(-Ag)}$ cm^{-2} achieved with a 2.6 $\mu g\ h^{-1}$ production rate, 6 Wh energy consumption, 0.9 m^3 Ar h^{-1} consumption) were produced and denoted as Cu–GO, Cu–NCB, Cu–Ag–GO and Cu–Ag–NCB. The sizes of the clusters produced in the aerosol were analysed with a differential mobility analyser, and the average sizes of the Cu and Cu–Ag clusters were determined to be 1.6 ± 0.2 and 1.5 ± 0.2 nm, respectively (Supplementary Figs. 2 and 3)[41]. After immobilizing the clusters on the carbon supports, their sizes were measured using high-angle annular dark-field scanning transmission electron microscopy (HAADF-STEM; Fig. 3 and Supplementary Figs. 4–8). The results indicated that the clusters were successfully stabilized as the measured sizes of the Cu and Cu–Ag clusters, 1.8 ± 0.7 and 1.4 ± 0.8 nm, respectively, compared well with the sizes in the aerosol (Fig. 2a,b, Supplementary Figs. 5, 7 and 8 and Supplementary Table 1). Interestingly, when N-edge functionalized graphene and multiwalled carbon nanotubes were used as control substrates, cluster agglomeration was observed (Supplementary Figs. 6 and 9). X-ray photoelectron spectroscopy (XPS) analysis of the supports indicates that the strength of the cluster–support interaction was not a measure of the support work function (Supplementary Fig. 10 and Supplementary Note 5). Instead, both the crystallinity and the amount of specific ligation sites explained the different cluster–support interactions and their respective (in)stability (Supplementary Figs. 11–16 and Supplementary Table 2). Furthermore, XPS analysis of the Cu(−Ag) clusters showed that both Cu and Ag were partially oxidized upon synthesis (Cu_xO_y and Ag_vO_w) but fully oxidized after 7 days of exposure to air existing as CuO and Ag_2O phases, respectively (Supplementary Fig. 17 and Supplementary Note 7). The presence of the Cu and Cu–Ag clusters was confirmed by STEM–energy-dispersive X-ray spectroscopy (EDXS; Fig. 3c,d). Furthermore, the average composition of the Cu–Ag clusters was determined to be $Cu_{84}Ag_{16}$ (at.%), which agrees well with the the surface composition obtained from XPS (Supplementary Note 7, Supplementary Fig. 17 and Supplementary Table 3).

To further understand the influence of the carbon support on the coordination structure and the chemical state of the clusters, we analysed the Cu-cluster-based catalysts using X-ray absorption spectroscopy (XAS; Fig. 2e–h) and compared them with the XPS results. The pseudo-radial distribution function extracted from the extended X-ray absorption fine structure (EXAFS) spectra excluded the presence of metallic Cu species, corroborating the XPS results of a CuO phase (Fig. 3e,f, Supplementary Note 8 and Supplementary Figs. 18 and 19). A Cu–O scattering event in the first coordination shell of CuO could be discerned for both the NCB- and GO-based catalysts. The Cu–O CNs for Cu–NCB and Cu–GO are 3.6 ± 0.3 and 3.2 ± 0.2 (compared with 4 in bulk CuO), respectively (Supplementary Tables 4 and 5), suggestive of a small particle size (expected CN ~3 for CuO clusters ~1 nm)[42,43]. Furthermore, we attribute the absence of information in the second coordination shell of Cu–GO to a stronger support–cluster interaction

https://doi.org/10.1038/s44160-024-00705-3

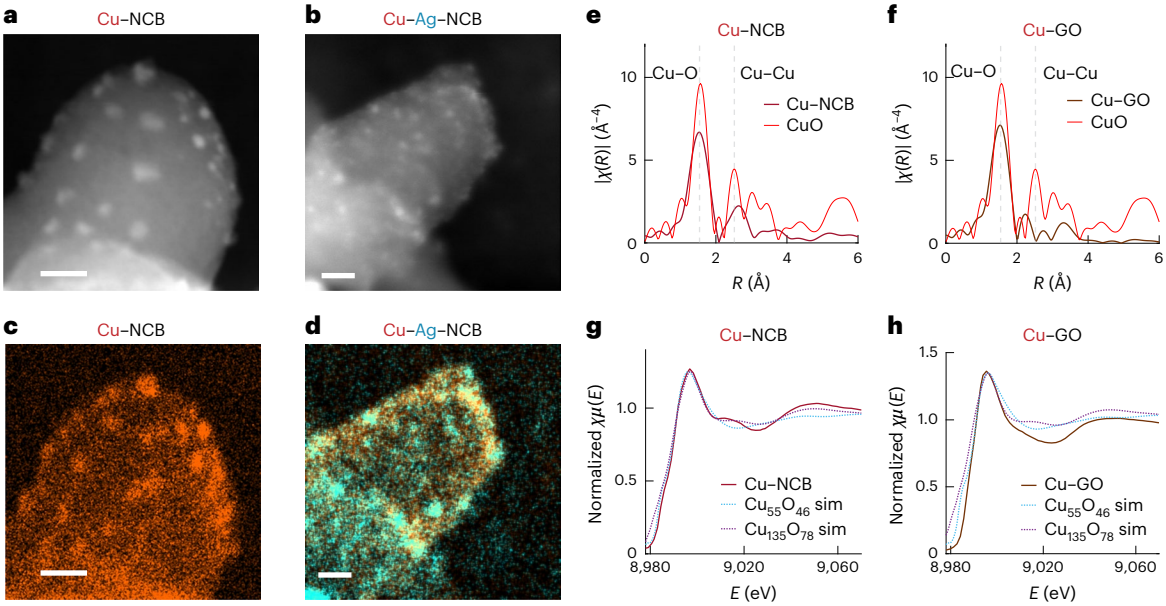

Fig. 3 | Advanced characterization of the as-synthesized Cu(–Ag) oxide clusters immobilized on heteroatom-doped carbonaceous support. a,**b**, HAADF-STEM images of the Cu–NCB and Cu–Ag–NCB catalyst. **c**,**d**, The corresponding STEM–EDXS elemental maps of **a** (**c**) and **b** (**d**), showing Cu in orange and Ag in turquois. Scale bars, 10 nm. **e**,**f**, Pseudo-radial distribution functions extracted from the EXAFS spectra of the Cu–NCB (**e**) and Cu–GO (**f**) catalyst. CuO powder was used as a reference. **g**,**h**, XANES spectra of the Cu–NCB (**g**) and Cu–GO (**h**) catalyst. XANES simulations of Cu-oxide clusters of various atomicity are offered as references for the particles. Sim, simulation. *E*, absorption edge energy in eV; *R*, interatomic distance in Å.

and its consequential loss of long-range order and/or the effects of static disorder dampening due to the varying bond lengths within the particle. GO has a higher density of ligation sites compared with NCB and can, therefore, form more bonds indicative of a potential stronger support interaction. This is consistent with the smaller CN of the corresponding cluster (Supplementary Fig. 12 and Supplementary Table 2). This behaviour shows similarities with a fully dispersed single-atom Cu catalyst also lacking long-range order[44–46]. Finally, we show by simulating the X-ray absorption near-edge structure spectroscopy (XANES) spectra of a series of Cu-oxide clusters including $Cu_{43}O_{24}$, $Cu_{55}O_{46}$ and $Cu_{135}O_{78}$ that the experimental XANES spectra show strong resemblance to oxidized Cu clusters of ~1 nm (Fig. 3g,h and Supplementary Fig. 20)[47]. Furthermore, the XANES spectra of the as-synthesized Cu-oxide clusters show limited resemblance to their bulk counterparts, confirming the need for better references to describe small cluster catalysts using XAS (Supplementary Fig. 21).

Electrochemical screening of the Cu-cluster precatalysts

We subjected our NCB- and GO-supported Cu(–Ag) cluster oxide precatalysts to a series of electrochemical screening tests to determine their activity in CO_2RR (Supplementary Note 9). Since support effects have been invoked to explain performance differences in Cu-cluster-based composites before[29,30], we deemed it of utmost importance to deconvolute the contribution of the support from that of the cluster. Therefore, we first determined the activity of the NCB and GO supports (Supplementary Figs. 22–25). The NCB powder showed over 90% Faradaic efficiency (FE) for CO, even at a modest overpotential of 600 mV (Supplementary Fig. 24a). However, the GO support produced H_2 as a majority product at all potentials tested (Supplementary Fig. 24b), with less than 20% FE towards $HCOO^-$ detected. The high CO selectivity of the NCB support could be attributed to the N-containing sites, which have been demonstrated to be favourable for CO_2-to-CO conversion in the past[48,49]. Alternatively, the higher hydrophobicity of NCB over GO may play a role as well[50]. Nevertheless, the strongly differentiating CO activities (2 mA cm^{-2} versus 40 μA cm^{-2} for NCB and GO, respectively; Supplementary Fig. 25) are expected to greatly influence the product distribution of the cluster–support composites.

With the activity of the supports quantified, the CO_2RR performance of Cu(–Ag) clusters could be investigated. Figure 4 shows the product distribution as a function of the potential, the support and the type of cluster. Independent of the support (Fig. 4a,b), acetaldehyde could be observed at any potential between −0.5 V and −1.1 V versus RHE upon the introduction of Cu-oxide clusters. Acetate and formate could also be detected as minor products (<10%). Only for the NCB-based samples was CO a notable product, especially at high overpotential, which clearly stems from the support activity. Furthermore, especially at lower overpotentials (more cathodic than −0.8 V versus RHE), significant acetaldehyde selectivity could be reported. For Cu–NCB at −0.5 V versus RHE, an acetaldehyde selectivity of 66 ± 20% was determined. At the same potential, for Cu–GO, the FE was as high as 92 ± 2%. For the NCB-based catalysts, increasing the overpotential by 100–200 mV, placed the acetaldehyde FEs in the 40–50% range. Likewise, for Cu–GO, the selectivity decreased to around 50% at −0.7 V versus RHE. Further increasing the overpotential reduced the acetaldehyde selectivity independently of the support, but the selectivity remained >10% up to −0.9 V versus RHE. Interestingly, upon the introduction of 16 at.% Ag into the clusters, a similar trend was observed as for pure Cu-oxide clusters (Fig. 4c,d). However, for the Cu–Ag–NCB catalyst, at −0.5 V versus RHE the FE towards acetaldehyde was as high as 88 ± 1%. The C_{2+} selectivity was approximately 100%. For the Cu–Ag–GO catalyst, a ~70% acetaldehyde selectivity could be maintained up to −0.7 V versus RHE. For the complete dataset of FEs, see Supplementary Tables 5–8. For the current densities, see Supplementary Fig. 26.

Since clusters are known to be mobile on carbon supports[29–31], we carefully examined the catalytic stability of our Cu-cluster catalysts to evaluate their potential in long-term operation (Fig. 4e and Supplementary Fig. 27). First, a second round of performance evaluation was performed on Cu–NCB catalysts that were subjected to several hours of air exposure (Fig. 4e, cycle 2). Notably, neither the current density (−148 μA cm^{-2}) nor the acetaldehyde selectivity (41%) changed. We then repeated this process but extended the reaction time tenfold to

https://doi.org/10.1038/s44160-024-00705-3

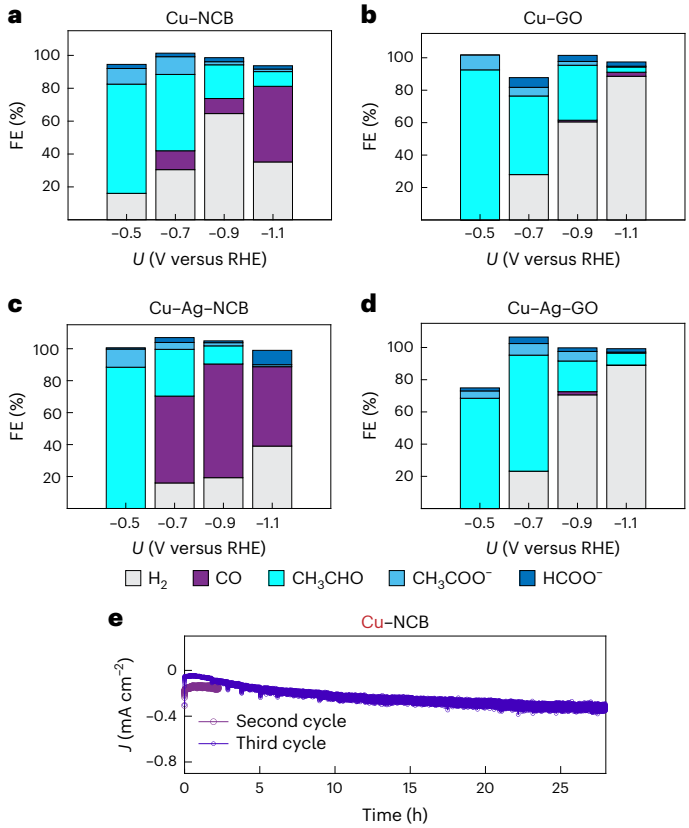

Fig. 4 | Electrocatalytic screening for CO_2 reduction to acetaldehyde. **a**,**b**, Selectivity screening of Cu–NCB (**a**) and Cu–GO (**b**) GDL composites. **c**,**d**, Selectivity screening of Cu–Ag–NCB (**c**) and Cu–Ag–GO (**d**) GDL composites. **e**, A stress test of the Cu–NCB catalyst at −0.6 V versus RHE, including three start–stop cycles and an overall operation time of >30 h. All electrochemical reactions were carried out in CO_2-saturated 0.1 M $KHCO_3$ electrolyte in a Nafion membrane-separated H-cell. Chronoamperometry was carried out in a cathodic potential window of −0.5 to −1.1 V versus RHE (half-cell potential, iR-drop corrected) using an Ag/AgCl reference electrode. A Pt foil (1 cm^2) was used as the counter electrode. Gaseous products were quantified via gas chromatography. Liquid products were detected using H-NMR and quantified using the protocol from Kuhl et al.[10]. For the lower-overpotential experiments (<800 mV), liquid products were collected for at least 3 h to ensure reliably measurable concentrations. For all other potentials, FEs were averaged for a minimum of 30 min. For the lower overpotential experiments (<800 mV), averages were reported of two independent measurements with FE ranges for Cu–NCB, Cu–GO, Cu–Ag–NCB and Cu–Ag–GO of 0–32%, 0–45%, 0–17% and 0–29% for H_2; 0–34%, 0%, 0–55% and 0% for CO; 46–86%, 30–94%, 26–86% and 64–74% for CH_3CHO; 8–14%, 2–9%, 4–11% and 2–18% for CH_3COO^- and 0–5%, 0–7%, 0–4% and 0–6% for $HCOO^-$, respectively. The less than 100% FE observed for the Cu–Ag–GO GDL at −0.5 V versus RHE stems from unquantifiable gaseous products due to dilution of the CO_2 stream (H_2 most likely). The reused Cu–NCB catalyst (E) offered a stable and comparable current density (−148 μA cm^{-2}) and acetaldehyde FE (41%; Supplementary Fig. 28), as observed for the first 3 h (−193 ± 45 μA cm^{-2} and 43 ± 22%, respectively; Supplementary Table 5 and Supplementary Fig. 27). H-NMR, proton nuclear magnetic resonance spectroscopy. *U*, half-cell potential in V; iR, loss of voltage or ohmic drop in which *i* denotes the current; *R*, the resistance; *J*, current density in mA cm^{-2}.

~30 h (Fig. 5, cycle 3). After an initial stage of equilibration (first 3 h), a stable performance was obtained, similar to the first and second cycle. Finally, we observed no significant change in the Cu metal loading before and after catalysis, corroborating the stability of the clusters (Supplementary Table 9). The absence of ethanol in the reaction mixture may seem surprising at first. It is well known that, under basic conditions, acetaldehyde undergoes a disproportionation reaction to ethanol and formate[51]. However, due to the strong buffering effect of the electrolyte (0.1 M $KHCO_3$), this disproportionation is limited. Indeed, very recent studies have shown that Cu single crystals produce acetaldehyde stably under buffering conditions but react further under alkaline conditions[52].

Electrochemically speaking, the cluster–support composites differ in two major ways: (1) NCB and GO are respectively good and poor CO_2RR electrocatalysts for the production of CO (refs. 48,49), which could explain differences in performance by means of tandem effects upon the introduction of the clusters[53], and (2) these samples have different cluster–support interactions of varying strength, that is, via N- and NO_x-ligation sites in the case of NCB and C=O, OH and COOH groups for GO, respectively, which may affect the performance, similarly to what has been observed for atomically precise ligand-capped Au clusters[54]. Clearly, our investigations show that the effect of the support is minor. Only when the support is active (<−0.7 V versus RHE) does it influence the product distribution. Furthermore, it does not affect the acetaldehyde pathways as the production distribution shows an enhanced rate only to its natural product: CO and H_2 for NCB and GO, respectively. Therefore, we conclude the absence of a tandem effect and confirm the cluster atomicity as the key driver in this reaction.

Formation of the active catalyst

To investigate the nature of the active species, we devised an in situ XAS experiment to monitor the chemical nature of the CuO cluster composite precatalysts. Following a previously reported procedure, we prepared a thin catalyst layer (~2 μm thick) of Cu–NCB on a carbon-sputtered Kapton foil to minimize mass transport effects and limit delamination under operation (Supplementary Table 10)[55–57]. Then, using an in-house-developed in situ spectroelectrochemical cell that is based on the design of Binninger et al.[58] and that allows measurements in grazing incidence geometries, the transient nature of the CuO cluster precatalyst was studied as a function of the potential under equivalent CO_2RR conditions (Fig. 5; CO_2-saturated 0.1 M $KHCO_3$, the potential was kept for 70 min for all measurements). Similar to the as-synthesized Cu–NCB catalyst, the catalyst at open circuit potential is fully oxidized, that is, Cu(II) (Fig. 5a). Upon applying a cathodic potential of −100 mV versus RHE, the XANES spectra indicates the formation of a Cu_2O phase. After further reduction to −200 mV, the Cu_2O phase starts to disappear and the metallic phase appears. At −300 mV versus RHE, a complete reduction of the Cu(I) to Cu(0) can be observed. Furthermore, a good agreement between the experimental results and the simulated XANES spectra of the relevant Cu-oxide clusters and their metallic face-centered cubic (FCC) counterparts can be observed (Fig. 5b). Finally, we exclude the presence of body-centered cubic (BCC) crystal structures reported previously, by means of simulation (Supplementary Fig. 28)[59]. For reasons of clarity, we show only a subset of the simulated XANES spectra of the particles. For the complete set, see Supplementary Fig. 29.

To investigate the atomic structure of the catalyst, we observed the pseudo-radial distribution function of the EXAFS spectra in the −100 and −300 mV versus RHE range (Fig. 5c). Indeed, a scattering event in the first coordination shell associated with the Cu_2O phase could be observed up to −200 mV versus RHE. However, at −300 mV versus RHE, this feature is completely absent. Instead, a Cu–Cu scattering event can be discerned of metallic Cu. Fitting of the Cu coordination shell estimates a Cu CN of 7.3 ± 3.3 (Supplementary Table 11 and Supplementary Fig. 30)[60]. We translate that into an average particle size of 1.2 nm (refs. 61,62), which is in excellent agreement with the as-synthesized CuO clusters (Fig. 2). Furthermore, we determine that the coordination bond has shortened by 0.10 Å with respect to the bulk, which is typically observed in clusters[63,64]. We can, thereby, conclude that the active species is indeed a metallic Cu cluster of an average atomicity of ~100 atoms, which agrees with the expected atomicity based on differential mobility analysis and HAADF-STEM and was identified

https://doi.org/10.1038/s44160-024-00705-3

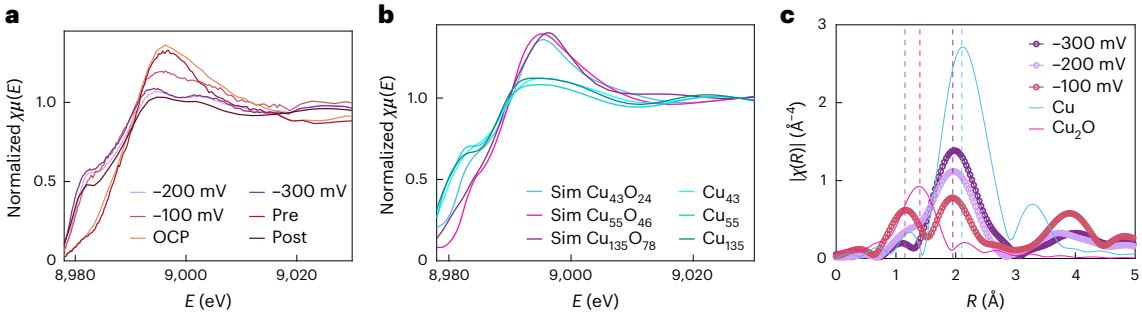

Fig. 5 | In situ activation of the precatalyst. a, In situ XANES spectra of the Cu–NCB catalyst in 0.1 M $KHCO_3$ as a function of the potential. Each spectrum depicted is an average of three acquired spectra (20 min each) used for signal-to-noise enhancement. **b**, Simulated XANES spectra of Cu-oxide and Cu metallic clusters of equivalent atomicity. **c**, In situ EXAFS spectra of the Cu–NCB catalyst in 0.1 M $KHCO_3$ between −100 mV and −300 mV versus RHE. Scattering paths of Cu_2O (powder) and Cu (foil) are offered as references. OCP, open circuit potential.

as promising through our computational method (Fig. 1 and Supplementary Figs. 2–5). Furthermore, we observe the catalyst used for the synchrotron experiments after catalysis using STEM and confirm that it retained small particle size of ~1 nm, further corroborating the stability of the catalyst (Supplementary Fig. 31).

Finally, out of curiosity, we investigated the oxidation state of Cu-cluster GDL catalyst composites after catalysis (Supplementary Figs. 32–34). Interestingly, the XAS spectra showed that the clusters had partially retained their metallic state even after exposure to air and independently of the support, that is, Cu–Cu CNs for NCB- and GO-supported Cu clusters are 6.2 + 1.4 and 7.4 ± 3.6, respectively (Supplementary Fig. 32a–c and Supplementary Tables 12 and 13). Again, the consistently small particle size of the clusters after reaction could be confirmed with STEM (Supplementary Fig. 31d). This confirms the earlier reported oxidation resistance of metallic Cu clusters[65] and may explain the stability of the catalysts.

Mechanistic studies

To understand the high selectivity for acetaldehyde and its early-onset potential, we simulated the CO_2RR pathways over the Cu_{43} cluster that exhibited the proposed active site (CN 11). Furthermore, we compared it with a cluster that lacked the proposed active site, that is, it filled by another Cu atom, Cu_{55}, using density functional theory (DFT; Fig. 6). Note that we have opted for the smallest cluster that manifested the coordination 11 sites (CN 11) to consider its mechanism at the highest level of theory. Our investigations reveal that, for either cluster, stable reductive adsorption of *CO through CO_2 (g) + *(sorption site) + $2(H^+ + e^-)$ → *CO + H_2O (l) is highly thermodynamically favourable but occurs at a much wider potential regime for Cu_{43} than for Cu_{55} (Fig. 6a,b; −0.34 to 0.18 V versus RHE versus −0.17 to 0.11 V versus RHE, respectively). Furthermore, for the majority of surface atoms (CNs 5 and 8), *CO binds tightly. Interestingly, only for the CN 11 surface sites, *CO exhibits an unstable binding mode, favouring its desorption (Fig. 6a). We argue that the high activity of our target cluster can be explained in two ways. First, for the target cluster, a wider potential window for favourable reduction of CO_2 to *CO exists, which results in a higher cluster coverage of *CO at more cathodic potentials, which enhances C–C coupling (as compared with a Cu(110) surface). Second, the last-formed *CO, which is on the CN 11 sites, is unstable, which prompts desorption and instigates the C–C coupling.

To elucidate the specific preference for acetaldehyde formation over ethanol and, notably, acetic acid—a preference that has been empirically correlated in the bulk[13,32]—we embarked on a comparative study with an extended (110) surface (Supplementary Fig. 35 and Supplementary Table 14). First, we show that unstable reductive *CO adsorption on the extended surface is feasible only at potentials lower than −1.05 V versus RHE, substantially more cathodic than for the clusters (Fig. 6a,b and Supplementary Fig. 35). Second, surface *CO coverage is predicted to saturate at half a monolayer, resulting in a substantially reduced surface *CO coverage compared with the cluster. We, therefore, posit that the increased *CO coverage observed on the cluster enhances the *CO coupling rate and contributes to an overall increased selectivity towards C_2 products as compared with the extended surface. Indeed, adsorbed *CO could be observed on the Cu–NCB catalyst in situ using attenuated total reflectance Fourier transform infrared spectroscopy and even at low overpotential (Supplementary Fig. 36a). Furthermore, enhancement of the attenuated total reflectance Fourier transform infrared spectra showed that not only atop-*CO but also bridged-*CO could be observed (Supplementary Fig. 36b), which has been correlated with higher C_{2+} production rates previously[1].

Then, assuming an initial state featuring two adjacent *CO adsorbates, we investigated the bifurcation of the plausible pathways on the cluster and the extended surface (Fig. 6c and Supplementary Fig. 35a–c). We propose a key transient intermediate, ketene ($H_2C{=}C{=}O$), to explain the difference between Cu_{43} and the extended (110) surface in terms of their tendency to form acetic acid, as it is substantially less stable on Cu(110). Concerning ethanol, we propose the difference in selectivity to arise from the stability of the *$COCH_3$ (associated with acetaldehyde) and *CH_2CHO (associated with ethanol) intermediates, respectively. Although for both the cluster and the Cu(110) surface *$COCH_3$ and *CH_2CHO form with comparative ease, the cluster favours the adsorption of *$COCH_3$, but Cu(110) prefers to stabilize *CH_2CHO. This difference leads us to surmise that the cluster is comparatively more inclined towards acetaldehyde than ethanol formation. Finally, we note that acetaldehyde can form on the clusters with 100 mV less cathodic than on Cu(110), which explains the experimentally determined early-onset potential. Unfortunately, no C_2-intermediate species could be observed in situ (Supplementary Fig. 36), probably due to their short-lived transient nature and the low current densities and, thus, overall surface concentrations.

Together, these results indicate that the Cu_{43} cluster exhibits similar active sites with the Cu(110) surface, favouring acetaldehyde formation, but is more prone to produce *CO and enables a higher surface coverage. Furthermore, the propensity towards acetaldehyde formation is stronger for the cluster compared with the extended surface and also at lower cathodic potentials. Moreover, we investigated the effect of the support on the adsorption of CO* and observed negligible differences (Supplementary Figs. 37 and 38).

Although we had expected Ag to play an important role in the reaction, we conclude that it is, at best, minor. The differences in selectivity are fully dominated by the reaction rates of the parasitic hydrogen evolution reaction (HER) and CO production of the supports and the atomicity of the clusters. In the absence of tandem effects, adding Ag does not enhance the C–C coupling rate and its only effect is electronical. In this system, adding Ag 16 at.% affects the electronics only

https://doi.org/10.1038/s44160-024-00705-3

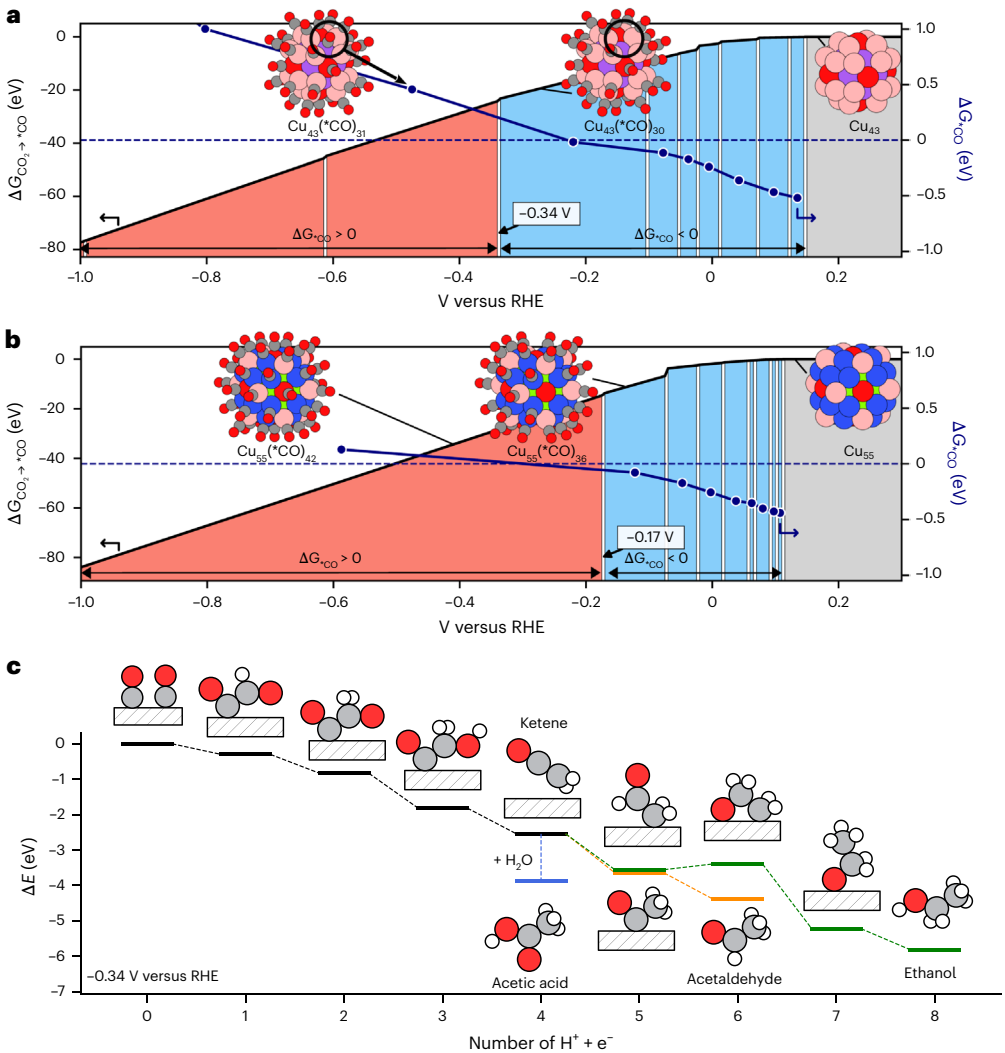

Fig. 6 | Mechanistic insight in the facile conversion of CO_2 to acetaldehyde on Cu clusters. a,**b**, Simulated energy profiles illustrating diverse *CO coverages on a Cu_{43} (**a**) and Cu_{55} (**b**) cluster obtained via CO_2 reduction, as a function of applied potential. The colour coding differentiates states with no adsorbed *CO, stably adsorbed *CO and unstably adsorbed *CO (grey, blue and red regions, respectively). Notably, for Cu_{43}, the onset of unstable *CO adsorption is predicted to manifest initially at the CN 11 atom. **c**, An energy diagram depicting a proposed reaction mechanism for acetaldehyde formation on the Cu_{43} cluster at the potential where the first instance of unstable *CO adsorption occurs. Δ*G*, Gibbs free energy change in eV.

marginally. For example, exchanging a Ag atom with a Cu 5, 8, 11 or 12 CN site changes the CO* adsorption energy by only ~0.1 eV (Supplementary Fig. 39). Furthermore, adding Ag beyond 16 at.%. would be detrimental to the performance as it would distort the active site. Therefore, it is considered outside of the scope of this work to include clusters with higher Ag content.

Conclusions

We have developed a computational target selection procedure and scalable production and immobilization method to produce bimetallic Cu-based clusters of sizes <2 nm. We propose that the spark ablation methodology can be scaled by two means: (1) via the enhancement of the spark repetition frequency, which generated higher ablation rates, and (2) via the utilization of a multitude of sources deployed in a parallel capacity similar to role-to-role printing strategies. We show that such composite materials have unique catalytic properties and show high selectivity towards acetaldehyde (>90%) in the electrochemical conversion of CO_2. We show that our catalysts retain their in-situ-formed metallic nature after catalysis and demonstrate that this feature offers resistance against potential cycling. We elucidate the conversion of CO_2 to acetaldehyde over the clusters using DFT and show its resemblance to the Cu(110) while clarifying that it enhances selectivity. We propose our catalyst target selection and production method as a platform technology that offers researchers a class of catalysts to screen for activity in various electrochemical reactions such as water splitting, oxygen evolution and nitrogen reduction.

Methods

Support substrate production

The NCB-based material was synthesized via a protocol adapted from Yang et al.[40]. In brief, Vulcan carbon black (FuelCellStore, 900 mg) was oxidized by means of mixing with an aqueous HNO_3 solution (Sigma-Aldrich ≥65%, 30 ml) and heated to 80 °C while stirring under reflux for 3 h. The oxidized carbon black was collected with 50 ml of water and washed until a neutral pH ~6.8 was reached. The washed product was dried overnight under vacuum of which 150 mg was mixed with urea in a mortar (Sigma-Aldrich >99%, 1.5 g). The mixture was placed in a ceramic boat and heated to 800 °C in 80 min, kept for 60 min at 800 °C and then cooled naturally to room temperature under Ar atmosphere. The 500 mg of NCB nanoparticles were washed and collected with *iso*-propanol (*i*PrOH) reaching a concentration of 30 mg ml^{-1}. GO nanoparticles were produced according to a previously

reported synthesis[39]. The synthesized supports were airbrushed on a 47 mm disc of carbon paper (Toray TGP H-60, Fuel Cell) at a 0.6 mg cm^{-2} and 0.3 mg cm^{-2} loading, respectively. For a detailed description of the support synthesis, see Supplementary Note 1.

Cluster production

The production of the Cu(−Ag) oxide clusters was achieved with a modified nanoparticle generator from VSParticle B.V. in which the capacitance was reduced 20-fold to 1 nF. A pin-to-hole electrode configuration was used. The flow rate of the carrier gas (Ar) was kept between 15 and 25 standard litres per minute. The overpressure was kept below 100 mbar. The sparking voltage was kept between 0.4 kV and 0.6 kV and the current kept at 2.5 mA. The clusters were collected on the support substrates by means of filtration. For a detailed description of the cluster production process, see Supplementary Note 2.

Electrode preparation

Circular sectors of the Cu–NCB and Cu–GO catalysts were cut out with a geometrical surface area of 0.5 cm^2. Finally, 20 µl of 0.83 wt.% Nafion dispersed in iPrOH was added as a binder.

Characterization

Electron microscopy. Scanning electron microscopy images were acquired with a Thermo Scientific Teneo. Transmission electron microscopy images were acquired using a Thermo Scientific Tecnai-Spirit with an acceleration voltage of 120 kV in bright-field mode. The instrument was equipped with a Gatan Orius charge-coupled device camera and Digital Micrograph software for imaging. Specimens were prepared on Au grids (400 mesh) from Ted Pella with ultrathin carbon film. Scanning transmission electron microscopy (STEM) was performed using a double Cs-corrected Tecnai-Osiris operated at 200 kV. This microscope is equipped with a Super-X EDX system, and high-brightness extended field emission gun (X-FEG) STEM images were obtained in the HAADF-STEM mode.

XPS. XPS was performed using a monochromated Al K_α (1,486.61 eV) X-ray source at a nominal power of 225 W on a Kratos Axis Supra system (the pressure in the analysis chamber base was kept at 1×10^{-9} mbar). A pass energy of 20 eV was used for acquiring all core-level and Auger electron spectra. The binding energies were referenced to Au $4f_{7/2}$ at 83.95 eV. The samples were drop-casted on a gold foil. No charge compensation was required as the samples were conductive.

Inductively coupled plasma mass spectrometry. Elemental analysis of the catalysts was achieved with a NexION 350D inductively coupled plasma mass spectrometry instrument from PerkinElmer. Digestion was achieved with concentrated HNO_3. The calibration curves were obtained through the preparation of a dilution series of elemental standards obtained from Sigma-Aldrich.

XAS. XAS measurements at the Cu K edge were performed at the SuperXAS beamline at the Swiss Light Source. The measurements were done with Si-coated collimating mirror at 2.9 mrad, Si(111) channel-cut monochromator and Rh-coated toroidal focusing mirror. The beam size on the sample was 150 × 150 μm^2. The beam intensity was monitored with three 15-cm-long ionization chambers filled with 2 bar N_2. The fluorescence signal was measured with a five-element silicon drift detector (SDD) brand-SGX and normalized to the intensity of the incident beam. All measurements were performed in grazing incidence configuration. Fitting of the spectra was achieved with the Athena/Artemis software package[60]. Fitting was performed in *k*-space from 3.0 to 9.5 $Å^{-1}$ and *R* space from 1.0 to 3.0 Å for all spectra. A Cu foil was mounted between the second and the third ionization chambers and used for precise energy calibration.

Attenuated total reflection surface-enhanced infrared absorption spectroscopy. In situ attenuated total reflection surface-enhanced infrared absorption spectroscopy measurements were performed on a Thermo Nicolet iS50 infrared spectrometer equipped with a liquid nitrogen-cooled mercury cadmium telluride detector, with a resolution of 2 cm^{-1} and 32 accumulated scans. A silicon crystal (with or without a chemically deposited gold film) was used for attenuated total reflection testing. Electrochemical measurements were conducted using a CHI660E potentiostat, with CO_2 purged 0.1 M $KHCO_3$ as the electrolyte, a saturated Ag/AgCl electrode as the reference electrode and a platinum foil as the counter electrode

DFT simulations

Structure relaxations. DFT simulations to obtain energies of structures were performed with the plane-wave implementation of the grid projector augmented wave (GPAW) software[66,67] version 22.1.0 in conjunction with the atomic simulation environment (ase)[33] version 3.22.1. The revised Perdew–Burke–Ernzerhof[68] exchange-correlation functional was used for obtaining energies. Clusters and molecules were relaxed in periodically repeated unit cells sized 25 × 25 × 25 Å using a Monkhorst–Pack sampled 2 × 2 × 2 *k*-point grid of the Brillouin zone and a Fermi–Dirac smearing of the electron occupation of 0.001 eV. Cu(110) structures were simulated as periodically repeated 2 × 2 × 5-atom-sized slabs with the positions of the three bottom layers fixed. Then, 10 Å of vacuum was added above and below, and 6 × 6 × 1 *k*-points were used. A plane-wave energy cutoff of 400 eV was applied in all simulations, and structure geometries were relaxed to a force below 0.05 eV $Å^{-1}$ on any atom. Free energies, when used, were obtained using the corrections given in Supplementary Table 14.

Simulated XANES spectra. Simulated Cu K-edge XANES spectra were obtained with the finite difference method near-edge structure (FDMNES) program[47] (4 April 2023 edition) on clusters relaxed with DFT and bulk reference structures of Cu(FCC), CuO and Cu_2O from the Crystallography Open Database[69–75]. An adsorbing atom cluster radius of 6.5 Å was used with the Green's function implementation of the FDMNES software. Supplementary Fig. 20 shows the result of other parameter choices.

Ethics statement

The research conducted in this work follows the code of conduct for scientific integrity as defined by the Swiss Academies of Arts and Sciences Code of conduct for scientific integrity (ref. 76).

Data availability

All data are available in the article and its Supplementary Information. Source data are provided with this paper.

Code availability

DFT-simulated atomic structures and scripts necessary for reproducing the simulated results have been made freely available at https://nano.ku.dk/english/research/theoretical-electrocatalysis/katladb/co2-to-acetaldehyde/.

References

1. Barton, J. L. Electrification of the chemical industry. *Science* **368**, 1181–1182 (2020).
2. Health Assessment Document for Acetaldehyde: Review Draft (U.S. Environmental Protection Agency, 1987).
3. Smidt, J. et al. Katalytische Umsetzungen von Olefinen an Platinmetall-Verbindungen Das Consortium-Verfahren zur Herstellung von Acetaldehyd. *Angew. Chem.* **71**, 176–182 (1959).
4. Jira, R. Acetaldehyde from ethylene—a retrospective on the discovery of the Wacker. *process. Angew. Chem. Int. Ed.* **48**, 9034–9037 (2009).

5. Smidt, J. et al. Olefins with palladium chloride catalysts. *Angew. Chem. Int. Ed.* https://doi.org/10.1002/anie.196200801 (1962).
6. Imbao, J., van Bokhoven, J. A., Clark, A. & Nachtegaal, M. Elucidating the mechanism of heterogeneous Wacker oxidation over Pd-Cu/zeolite Y by transient XAS. *Nat. Commun.* **11**, 1118 (2020).
7. Fan, L. et al. Strategies in catalysts and electrolyzer design for electrochemical CO_2 reduction toward C_{2+} products. *Sci. Adv.* https://doi.org/10.1126/sciadv.aay3111 (2020).
8. De Luna, P. et al. What would it take for renewably powered electrosynthesis to displace petrochemical processes? *Science* **364**, eaav3506 (2019).
9. Nitopi, S. et al. Progress and perspectives of electrochemical CO_2 reduction on copper in aqueous electrolyte. *Chem. Rev.* **119**, 7610–7672 (2019).
10. Kuhl, K. P., Cave, E. R., Abram, D. N. & Jaramillo, T. F. New insights into the electrochemical reduction of carbon dioxide on metallic copper surfaces. *Energy Environ. Sci.* **5**, 7050–7059 (2012).
11. Hori, Y., Murata, A., Takahashi, R. & Suzuki, S. Electroreduction of carbon monoxide to methane and ethylene at a copper electrode in aqueous solutions at ambient temperature and pressure. *J. Am. Chem. Soc.* **109**, 5022–5023 (1987).
12. Hori, Y., Murata, A. & Takahashi, R. Formation of hydrocarbons in the electrochemical reduction of carbon dioxide at a copper electrode in aqueous solution. *J. Chem. Soc. Faraday Trans. 1* **85**, 2309–2326 (1989).
13. Hori, Y., Takahashi, I., Koga, O. & Hoshi, N. Electrochemical reduction of carbon dioxide at various series of copper single crystal electrodes. *J. Mol. Catal. A* **199**, 39–47 (2003).
14. Hori, Y. in *Modern Aspects of Electrochemistry* Vol. 42 (eds Vayenas, C. G. et al.) 89–189 (Springer, 2008).
15. Takahashi, I., Koga, O., Hoshi, N. & Hori, Y. Electrochemical reduction of CO_2 at copper single crystal Cu(S)-[*n*(111)×(111)] and Cu(S)-[*n*(110)×(100)] electrodes. *J. Electroanal. Chem.* **533**, 135–143 (2002).
16. Piqué, O., Low, Q. H., Handoko, A. D., Yeo, B. S. & Calle-Vallejo, F. Selectivity map for the late stages of CO and CO_2 reduction to C_2 species on copper electrodes. *Angew. Chem. Int. Ed.* **60**, 10784–10790 (2021).
17. Schouten, K. J. P., Qin, Z., Pérez Gallent, E. & Koper, M. T. M. Two pathways for the formation of ethylene in CO reduction on single-crystal copper electrodes. *J. Am. Chem. Soc.* **134**, 9864–9867 (2012).
18. Li, C. W. & Kanan, M. W. CO_2 reduction at low overpotential on Cu electrodes resulting from the reduction of thick Cu_2O films. *J. Am. Chem. Soc.* **134**, 7231–7234 (2012).
19. Chen, Z. et al. Grain-boundary-rich copper for efficient solar-driven electrochemical CO_2 reduction to ethylene and ethanol. *J. Am. Chem. Soc.* **142**, 6878–6883 (2020).
20. Wang, Y. et al. Catalyst synthesis under CO_2 electroreduction favours faceting and promotes renewable fuels electrosynthesis. *Nat. Catal.* **3**, 98–106 (2020).
21. Zhu, C. et al. Product-specific active site motifs of Cu for electrochemical CO_2 reduction. *Chem* **7**, 406–420 (2021).
22. Timoshenko, J. et al. Steering the structure and selectivity of CO_2 electroreduction catalysts by potential pulses. *Nat. Catal.* **5**, 259–267 (2022).
23. Batchelor, T. A. A. et al. High-entropy alloys as a discovery platform for electrocatalysis. *Joule* **3**, 834–845 (2019).
24. Ma, S. et al. Electroreduction of carbon dioxide to hydrocarbons using bimetallic Cu–Pd catalysts with different mixing patterns. *J. Am. Chem. Soc.* **139**, 47–50 (2017).
25. Hoang, T. T. H. et al. Nanoporous copper–silver alloys by additive-controlled electrodeposition for the selective electroreduction of CO_2 to ethylene and ethanol. *J. Am. Chem. Soc.* **140**, 5791–5797 (2018).
26. Zhong, M. et al. Accelerated discovery of CO_2 electrocatalysts using active machine learning. *Nature* **581**, 178–183 (2020).
27. Koolen, C. D. et al. Low-temperature non-equilibrium synthesis of anisotropic multimetallic nanosurface alloys for electrochemical CO_2 reduction. *Nat. Synth.* https://doi.org/10.1038/s44160-023-00387-3 (2023).
28. Koolen, C. D., Luo, W. & Züttel, A. From single crystal to single atom catalysts: structural factors influencing the performance of metal catalysts for CO_2 electroreduction. *ACS Catal.* https://doi.org/10.1021/acscatal.2c03842 (2022).
29. Karapinar, D. et al. Electroreduction of CO_2 on single-site copper–nitrogen-doped carbon material: selective formation of ethanol and reversible restructuration of the metal sites. *Angew. Chem. Int. Ed.* **58**, 15098–15103 (2019).
30. Xu, H. et al. Highly selective electrocatalytic CO_2 reduction to ethanol by metallic clusters dynamically formed from atomically dispersed copper. *Nat. Energy* **5**, 623–632 (2020).
31. Su, X. et al. Complementary operando spectroscopy identification of in-situ generated metastable charge-asymmetry Cu_2–CuN_3 clusters for CO_2 reduction to ethanol. *Nat. Commun.* **13**, 1322 (2022).
32. Bagger, A., Ju, W., Varela, A. S., Strasser, P. & Rossmeisl, J. Electrochemical CO_2 reduction: classifying Cu facets. *ACS Catal.* **9**, 7894–7899 (2019).
33. Larsen, A. H. et al. The atomic simulation environment—a Python library for working with atoms. *J. Phys. Condens. Matter* **29**, 273002 (2017).
34. Tran, R. et al. Surface energies of elemental crystals. *Sci. Data* **3**, 160080 (2016).
35. Schmidt-Ott, A. *Spark Ablation: Building Blocks for Nanotechnology* (Jenny Stanford Publishing, 2020).
36. Reinmann, R. & Akram, M. Temporal investigation of a fast spark discharge in chemically inert gases. *J. Phys. D* **30**, 1125 (1997).
37. Schwyn, S., Garwin, E. & Schmidt-Ott, A. Aerosol generation by spark discharge. *J. Aerosol Sci.* **19**, 639–642 (1988).
38. Maisser, A., Barmpounis, K., Attoui, M. B., Biskos, G. & Schmidt-Ott, A. Atomic cluster generation with an atmospheric pressure spark discharge generator. *Aerosol Sci. Technol.* **49**, 886–894 (2015).
39. Lee, D. C., Yang, H. N., Park, S. H. & Kim, W. J. Nafion/graphene oxide composite membranes for low humidifying polymer electrolyte membrane fuel cell. *J. Membr. Sci.* **452**, 20–28 (2014).
40. Yang, F. et al. Highly efficient CO_2 electroreduction on ZnN_4-based single-atom catalyst. *Angew. Chem. Int. Ed.* **57**, 12303–12307 (2018).
41. Chen, D.-R. et al. Design and evaluation of a nanometer aerosol differential mobility analyzer (Nano-DMA). *J. Aerosol Sci.* **29**, 497–509 (1998).
42. Liu, Y. et al. Mapping XANES spectra on structural descriptors of copper oxide clusters using supervised machine learning. *J. Chem. Phys.* **151**, 164201 (2019).
43. Nan, B. et al. Copper oxide clusters modified by bismuth single atoms to catalyze CO oxidation. *Appl. Catal. Gen.* **636**, 118578 (2022).
44. Yang, H. et al. Scalable production of efficient single-atom copper decorated carbon membranes for CO_2 electroreduction to methanol. *J. Am. Chem. Soc.* **141**, 12717–12723 (2019).
45. Guan, A. et al. Boosting CO_2 electroreduction to CH_4 via tuning neighboring single-copper sites. *ACS Energy Lett.* **5**, 1044–1053 (2020).
46. Zhao, K. et al. Selective electroreduction of CO_2 to acetone by single copper atoms anchored on N-doped porous carbon. *Nat. Commun.* **11**, 2455 (2020).
47. Bunău, O. & Joly, Y. Self-consistent aspects of X-ray absorption calculations. *J. Phys. Condens. Matter* **21**, 345501 (2009).

48. Hursán, D. et al. Morphological attributes govern carbon dioxide reduction on N-doped carbon electrodes. *Joule* **3**, 1719–1733 (2019).
49. Hursán, D. et al. CO_2 conversion on N-doped carbon catalysts via thermo- and electrocatalysis: role of C–NO_x moieties. *ACS Catal.* **12**, 10127–10140 (2022).
50. Pham, T. H. M. et al. Enhanced electrocatalytic CO_2 reduction to C_{2+} products by adjusting the local reaction environment with polymer binders. *Adv. Energy Mater.* **12**, 2103663 (2022).
51. Birdja, Y. Y. & Koper, M. T. M. The importance of Cannizzaro-type reactions during electrocatalytic reduction of carbon dioxide. *J. Am. Chem. Soc.* **139**, 2030–2034 (2017).
52. Qiao, Y., Hochfilzer, D., Kibsgaard, J., Chorkendorff, I. & Seger, B. Real-time detection of acetaldehyde in electrochemical CO reduction on Cu single crystals. *ACS Energy Lett.* **9**, 880–887 (2024).
53. Meng, D.-L. et al. Highly selective tandem electroreduction of CO_2 to ethylene over atomically isolated nickel–nitrogen site/copper nanoparticle catalysts. *Angew. Chem. Int. Ed.* **60**, 25485–25492 (2021).
54. Li, S. et al. Boosting CO_2 electrochemical reduction with atomically precise surface modification on gold nanoclusters. *Angew. Chem. Int. Ed.* **60**, 6351–6356 (2021).
55. Povia, M. et al. Combining SAXS and XAS to study the operando degradation of carbon-supported Pt-nanoparticle fuel cell catalysts. *ACS Catal.* **8**, 7000–7015 (2018).
56. Diercks, J. S. et al. Spectroscopy vs. electrochemistry: catalyst layer thickness effects on operando/in situ measurements. *Angew. Chem. Int. Ed.* **62**, e202216633 (2023).
57. Diklić, N. et al. Potential pitfalls in the operando XAS study of oxygen evolution electrocatalysts. *ACS Energy Lett* **7**, 1735–1740 (2022).
58. Binninger, T. et al. Electrochemical flow-cell setup for in situ X-ray investigations: I. Cell for SAXS and XAS at synchrotron facilities. *J. Electrochem. Soc.* **163**, H906–H912 (2016).
59. Alfke, J. L. et al. BCC–Cu nanoparticles: from a transient to a stable allotrope by tuning size and reaction conditions. *Phys. Chem. Chem. Phys.* **24**, 24429–24438 (2022).
60. Ravel, B. & Newville, M. ATHENA, ARTEMIS, HEPHAESTUS: data analysis for X-ray absorption spectroscopy using IFEFFIT. *J. Synchrotron. Rad.* **12**, 537–541 (2005).
61. Frenkel, A. Solving the 3D structure of metal nanoparticles. *Z. Krist. Cryst. Mater.* **222**, 605–611 (2007).
62. Marinkovic, N. S., Sasaki, K. & Adzic, R. R. Determination of single- and multi-component nanoparticle sizes by X-ray absorption spectroscopy. *J. Electrochem. Soc.* **165**, J3222 (2018).
63. Yamazoe, S. et al. Hierarchy of bond stiffnesses within icosahedral-based gold clusters protected by thiolates. *Nat. Commun.* **7**, 10414 (2016).
64. Apai, G., Hamilton, J. F., Stohr, J. & Thompson, A. Extended X-ray—absorption fine structure of small Cu and Ni clusters: binding-energy and bond-length changes with cluster size. *Phys. Rev. Lett.* **43**, 165–169 (1979).
65. Cook, A. W., Jones, Z. R., Wu, G., Scott, S. L. & Hayton, T. W. An organometallic Cu_{20} nanocluster: synthesis, characterization, immobilization on silica, and 'click' chemistry. *J. Am. Chem. Soc.* **140**, 394–400 (2018).
66. Mortensen, J. J., Hansen, L. B. & Jacobsen, K. W. Real-space grid implementation of the projector augmented wave method. *Phys. Rev. B* **71**, 035109 (2005).
67. Enkovaara, J. et al. Electronic structure calculations with GPAW: a real-space implementation of the projector augmented-wave method. *J. Phys. Condens. Matter* **22**, 253202 (2010).
68. Hammer, B., Hansen, L. B. & Nørskov, J. K. Improved adsorption energetics within density-functional theory using revised Perdew–Burke–Ernzerhof functionals. *Phys. Rev. B* **59**, 7413–7421 (1999).
69. Merkys, A. et al. Graph isomorphism-based algorithm for cross-checking chemical and crystallographic descriptions. *J. Cheminform.* **15**, 25 (2023).
70. Vaitkus, A., Merkys, A. & Gražulis, S. Validation of the crystallography open database using the crystallographic information framework. *J. Appl. Cryst.* **54**, 661–672 (2021).
71. Quirós, M., Gražulis, S., Girdzijauskaitė, S., Merkys, A. & Vaitkus, A. Using SMILES strings for the description of chemical connectivity in the Crystallography Open Database. *J. Cheminform.* **10**, 23 (2018).
72. Merkys, A. et al. COD::CIF::Parser: an error-correcting CIF parser for the Perl language. *J. Appl. Crystallogr.* **49**, 292–301 (2016).
73. Gražulis, S., Merkys, A., Vaitkus, A. & Okulič-Kazarinas, M. Computing stoichiometric molecular composition from crystal structures. *J. Appl. Cryst.* **48**, 85–91 (2015).
74. Gražulis, S. et al. Crystallography Open Database (COD): an open-access collection of crystal structures and platform for world-wide collaboration. *Nucleic Acids Res.* **40**, D420–D427 (2012).
75. Downs, R. T. & Hall-Wallace, M. The American Mineralogist crystal structure database. *Am. Mineral.* **88**, 247–250 (2003).
76. Aebi-Müller, R. E. et al. Code of conduct for scientific integrity. *Zenodo* https://doi.org/10.5281/zenodo.4707560 (2021).
77. Feng, J., Biskos, G. & Schmidt-Ott, A. Toward industrial scale synthesis of ultrapure singlet nanoparticles with controllable sizes in a continuous gas-phase process. *Sci. Rep.* **5**, 15788 (2015).
78. Feng, J. et al. General approach to the evolution of singlet nanoparticles from a rapidly quenched point source. *J. Phys. Chem. C* **120**, 621–630 (2016).
79. Preger, C., Overgaard, N. C., Messing, M. E. & Magnusson, M. H. Predicting the deposition spot radius and the nanoparticle concentration distribution in an electrostatic precipitator. *Aerosol Sci. Technol.* **54**, 718–728 (2020).
80. Megyeri, D., Kohut, A. & Geretovszky, Z. Effect of flow geometry on the nanoparticle output of a spark discharge generator. *J. Aerosol Sci.* **154**, 105758 (2021).
81. Feng, J., Ramlawi, N., Biskos, G. & Schmidt-Ott, A. Internally mixed nanoparticles from oscillatory spark ablation between electrodes of different materials. *Aerosol Sci. Technol.* **52**, 505–514 (2018).
82. Feng, J. et al. Unconventional alloys confined in nanoparticles: building blocks for new matter. *Matter* **3**, 1646–1663 (2020).
83. Tabrizi, N. S., Xu, Q., van der Pers, N. M. & Schmidt-Ott, A. Generation of mixed metallic nanoparticles from immiscible metals by spark discharge. *J. Nanopart. Res.* **12**, 247–259 (2010).
84. Voloshko, A. & Itina, T. E. in *Nanoparticles Technology* (ed. Aliofkhazraei, M.) Ch. 1 (IntechOpen, 2015).
85. Feng, J. *Scalable Spark Ablation Synthesis of Nanoparticles: Fundamental Considerations and Application in Textile Nanofinishing*. PhD Thesis, Delft Univ. Technology (2016).

Acknowledgements

This research was supported by Swiss National Science Foundation (Ambizione Project PZ00P2_179989, W.L.). The in situ XAS cell used in this work was developed in the framework of the European Union's Horizon 2020 research and innovation programme under the Marie Sklodowska-Curie grant agreement number 955650 (O.V.S. and J.H.). We acknowledge the financial support from China Scholarship Council (grant number 201506060156, M.L). We acknowledge support from the Danish National Research Foundation Center for High Entropy Alloy Catalysis (CHEAC) DNRF-149 (J.K.P.). We acknowledge the financial support by the Swiss National Foundation (project 184817, A.A.) and the Energy Systems Integration (ESI) Platform at the Paul Scherrer Institute. We also thank C. Ludwig of the Bioenergy and Catalysis Laboratory (LBK), Energy and Environment Research Division (ENE), Paul Scherrer Institute (PSI) and the School

of Architecture, Civil, and Environmental Engineering (ENAC IIE GR-LUD), École Polytechnique Fédérale de Lausanne (EPFL), Lausanne, Switzerland for the lively discussions. L. Menin and N. Gasilova of the Mass Spectrometry and Elemental Analysis Platform (MSEAP), Institute of Chemical Sciences and Engineering (ISIC), Basic Science Faculty (SB), École Polytechnique Fédérale de Lausanne (EPFL) Valais/Wallis, Energypolis, Sion, Switzerland, are acknowledged for their facilitation of the inductively coupled plasma mass spectrometry measurements. B. Boshuizen of Faculty of Applied Sciences Technical University of Delft, Delft, the Netherlands, is acknowledged for his XPS measurement of Cu(–Ag) oxide catalysts after production. A. Bornet of the Nuclear Magnetic Resonance Platform, Institute of Chemical Sciences and Engineering (ISIC), Basic Science Faculty (SB), École polytechnique fédérale de Lausanne (EPFL), Switzerland, is acknowledged for his assistance with H-NMR experiments. Y. Ko, Y. Wang and L. Zhong of the Laboratory of Materials for Renewable Energy (LMER), Institute of Chemical Sciences and Engineering (ISIC), Basic Science Faculty (SB), École polytechnique fédérale de Lausanne (EPFL) Valais/Wallis, Energypolis, Sion, Switzerland, are acknowledged for their assistance with the GO synthesis protocol, their assistance with the Brunauer-Emmett-Teller (BET) measurements and the design of Fig. 2 and contribution to XPS measurements, respectively. We acknowledge A. H. Clark of the Paul Scherrer Institute, CH-5232 Villigen PSI, Switzerland, for his support during the in situ synchrotron experiment. Finally, we acknowledge J. Rossmeisl of the Center for High Entropy Alloy Catalysis, Department of Chemistry, University of Copenhagen, Copenhagen, Denmark, for initial discussions on the design of the DFT simulations. Graphical abstract adapted with permission from ref. 28, American Chemical Society.

Author contributions

C.D.K. and J.K.P. conceptualized the project. C.D.K., W.L. and A.Z. supervised the project. C.D.K. and B.Z. developed the cluster production and associated characterization with contributions from T.V.P., W.V. and A.S.-O. C.D.K. developed the catalyst synthesis, characterization and related data processing. C.D.K. performed and interpretated the electrochemical tests with contributions from J.Z. W.L. and M.L. performed the XPS analysis and data treatment with contributions from Y.K. C.D.K., M.W., A.A., J.Z., J.H. and O.V.S. designed the in situ XAS experiments. M.W. and J.H. provided the spectroelectrochemical cell. C.D.K., M.W., A.A., Z.A. and Y.K. performed the in situ XAS experiment. O.V.S. performed the ex situ XAS experiments. C.D.K. performed the data treatment of XAS experiments with contributions from M.W. and O.V.S. J.K.P performed all DFT simulations. C.D.K., J.K.P. and W.L. co-wrote the paper. All the authors discussed the results and revised the paper. Questions regarding the synthesis, catalysis and characterization should be directed to C.D.K. All questions related to the DFT simulation should be directed to J.K.P.

Competing interests

This technology is part of a patent application (PCT/EP2024/058885). C.D.K. has become an advisor of VSParticle B.V. as a direct result of this collaboration. T.V.P. and A.S.-O. are founders of VSParticle B.V. B.Z. and W.V. are former employees of VSParticle B.V. The other authors declare no competing interests.

Additional information

Extended data is available for this paper at https://doi.org/10.1038/s44160-024-00705-3.

Supplementary information The online version contains supplementary material available at https://doi.org/10.1038/s44160-024-00705-3.

Correspondence and requests for materials should be addressed to Cedric David Koolen, Jack Kirk Pedersen or Wen Luo.

Peer review information *Nature Synthesis* thanks Yan Zhao and the other, anonymous, reviewer(s) for their contribution to the peer review of this work. Primary Handling Editor: Thomas West, in collaboration with the *Nature Synthesis* team.

https://doi.org/10.1038/s44160-024-00705-3

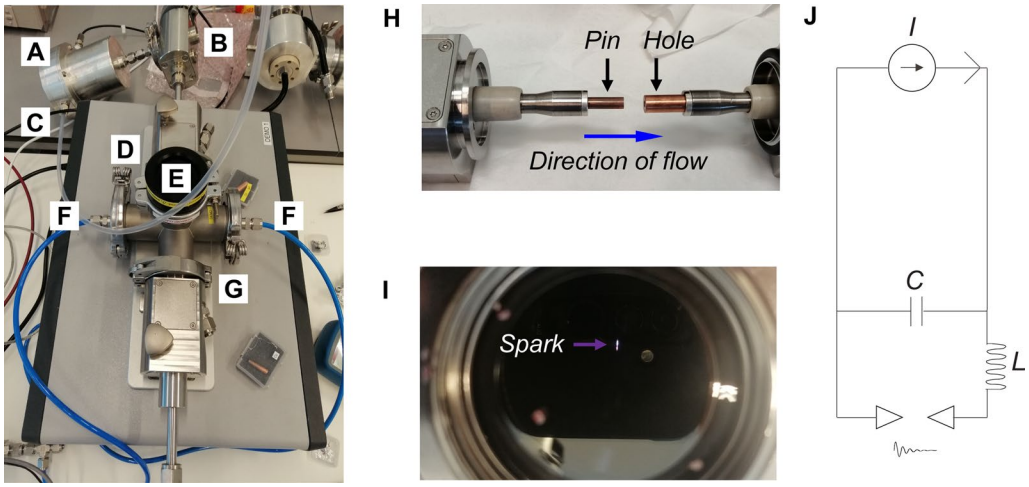

Extended Data Fig. 1 | Description of the spark ablation and electrostatic deposition experimental set-up, operation, and electrical components. (**a**) Faraday cup used to collect either negatively or positively charged particles from the aerosol. The measured current (via an electrometer) allows to determine the number of ions hitting the cup per unit of time giving a measure of the ablation rate (cluster production rate)[77,78]. (**b**) Deposition chamber allowing for a filter deposition in which the entire aerosol flow is passed through a substrate as well as an electrostatic deposition method in which a bias is applied to a substrate and as such only particles of opposite polarity are adhered to it[79]. (**c**) Aerosol exhaust. (**d**) Positive electrode (grounded). (**e**) Spark chamber. (**f**) Carrier gas (Ar) flow inlet. Direction of flow is from (E) to (B). (**g**) Negative electrode. (**h**) Pin-to-hole configuration of the electrode set-up of the spark ablator showing two Cu electrodes[80]. Exchanging the pin or negative electrode for Ag allows for the production of bimetallic clusters[81–84]. (**i**) Picture of the spark in operation. (**j**) Resistance-inductance-capacitance (RLC) electrical circuit, in which *I* denote the power supply. *C* denote(s) the capacitor, *L* denotes the inductor needed to store potential energy via the magnetic field needed for the oscillatory nature of the spark[85]. The spark is indicated by the damped exponential with a ~100 ns time constant of the oscillation of the spark between the grounded and negative electrode.